Nenjiang Formation deposits responses to astronomically forced climate changes during the Upper Cretaceous Songliao Basin

Yubin Guo[1], Jinyou He[1], Shaobin Guo[1]

[1]School of Energy resource, China University of Geosciences (Beijing), Beijing, 100083, China

5   *Correspondence to*: Jinyou He (hejinyou@cugb.edu.cn)

Abstract. The Songliao Basin preserves a complete Cretaceous continental sedimentary succession. Previous researchers have conducted extensive cyclostratigraphic studies on the Upper Cretaceous Nenjiang Formation, but paleoclimatic research has primarily focused on the lower part of the formation. The relationship between climatic changes and astronomical parameters in the middle and upper sections of the Nenjiang Formation has not yet been fully investigated. This

10   study conducted cyclostratigraphic analysis of the second to third members of Nenjiang Formation Late Cretaceous(K_2n^{2-3}) in the Songliao Basin using high-resolution gamma-ray logging (GR) data, while also performing paleoclimatic analysis in conjunction with palynological data. The fossil spores and pollen from the K_2n^3 indicate a geological age of the Late Cretaceous Campanian. Based on the ecological data of the parent plants of the spores and pollen, the vegetation types, climatic zones, and humidity types of the lower part of the K_2n^3 were analyzed, confirming its semi-warm and semi-humid

15   paleoclimatic characteristics.Time-series analysis reveals persistent 405-kyr (long eccentricity), 95-kyr (short eccentricity), 38.3-kyr (obliquity), and 22.8-kyr (precession) sedimentary cycles, further validated by an optimal sedimentation rate model. We established a 3.24-Myr floating astronomical time scale for K_2n^{2-3} by tuning the GR series to orbital targets. This timescale is anchored by a volcanic ash age (83.269 ± 0.044 Ma) at the K_2n^2 base, generating an absolute age framework spanning 83.33–80.00 Ma. Vertical transitions in palynofloral assemblages correspond to the 38.3-kyr obliquity cycle,

20   indicating significant obliquity forcing on regional paleoclimate dynamics.

1 Introduction

Gravitational interactions within the Solar System induce gradual alterations to Earth's rotational and orbital trajectories. These changes produce periodic variations in Earth's orbital parameters—primarily eccentricity, obliquity, and precession (Hinnov, 2013). The cyclical modulation of these parameters alters both the total solar insolation received by Earth and its

25   latitudinal and seasonal distribution, thereby driving global climate fluctuations on multimillennial (10,000years) scales (Milankovitch, 1941). Hays et al., (1976) employed spectral analysis on deep-sea sediment records and insolation data, revealing consistent precession (~23 kyr) and obliquity (~41 kyr) cycles persisting over 400,000 years. This work definitively established the relationship between orbital variations and Quaternary climate change, forming the cornerstone of cyclostratigraphy.

30 Wu et al., (2007) conducted spectral analysis of natural gamma-ray logs from the K_2qn and K_2n^{1-2} in the Songliao Basin, confirming that Late Cretaceous sedimentary cycles were controlled by Milankovitch climate forcing. Wu et al., (2014) and Ma et al., (2020) subsequently performed cyclostratigraphic analysis on Th spectral data from the SK-1n and Sk-2 boreholes, establishing an astronomical time scale. However, the sedimentation rates they derived for the K_2n^{2-3} differed significantly and lacked validation from other paleoclimate proxy indicators. Yang et al., (2020) and Li et al., (2022) combined high-

35 resolution elemental geochemical data to demonstrate that sedimentary cycles from the K_2n^{1-2} were driven by Milankovitch climate forcing, though the K_2n^3 was not addressed. Pollen fossils play a significant role in paleoclimate studies. Previous research on pollen fossils from the Nenjiang Formation in the Songliao Basin has established that the K_2n^{2-3} represent a warm and humid climate (Tian et al., 2005; Yan et al., 2007; Jing et al., 2011; Hinnov, 2013; Zhao et al., 2014; Zhou et al., 2023).

40 This study utilizes gamma-ray (GR) logging data from borehole G651 within the second and third members of the Nenjiang Formation for cyclostratigraphic analysis, aiming to identify astronomical forcing mechanisms and establish an astronomically calibrated timescale. In addition, palynomorph assemblages are analyzed to determine paleoenvironmental characteristics of the K_2n^3, with integrated cyclostratigraphic assessment of periodic paleoclimate drivers.

2 Geological Setting

45 The Songliao Basin, located in northeastern China (Figure 1a), has a length of approximately 500 km and a width of 330–370 km, covering an area of ~260,000 km². During the Cretaceous, it occupied a mid-to-high paleolatitude position in the Northern Hemisphere (Sewall et al., 2007). Stratigraphic architecture subdivides the basin into six first-order tectonic units: the Northern Tilted Zone, Central Depression Zone, Northeastern Uplift Zone, Southeastern Uplift Zone, Southwestern Uplift Zone, and Western Slope Zone (Figure 1b; Wang et al., 2013; Wu et al., 2023). The basin contains Jurassic,

50 Cretaceous, Paleogene, and Neogene strata, with Cretaceous successions constituting the dominant sedimentary fill.

The basement comprises Paleozoic metamorphic and igneous rocks. The sedimentary succession is divided into three tectonostratigraphic stages: 1) the fault depression stage (Early Cretaceous), including the Huoshiling (K_1h), Shahezi (K_1sh), and Yingcheng (K_1yc) Formations; 2) the depression stage (Cretaceous), containing the Denglouku (K_1d), Quantou (K_2q), Qingshankou (K_2qn), Yaojia (K_2y), and Nenjiang (K_2n) Formations; and 3) the tectonic inversion stage (Late Cretaceous),

55 including the Sifangtai (K_2s), Mingshui (K_2m), and Yi'an Formations (Feng et al., 2010; Li et al., 2021).

The K_2n^1 and K_2n^2 consist predominantly of dark mudstones, black shales, and oil shale interbeds, indicative of deep-lacustrine deposition. K_2n^3 and K_2n^4 record a shift to shallow-lacustrine and deltaic facies, while K_2n^5 comprises meandering river deposits, collectively forming a basin-fill succession transitioning from deep-water to shallow-water to subaerial environments. The lithologic assemblages of the K_2n^3 and the K_2n^4 are similar. The K_2n^3 consists of interbedded grayish-

60 black silty mudstone and mudstone with grayish-white argillaceous siltstone and sandstone. The K_2n^4 is composed of interbedded grayish-green and grayish-white sandstone and siltstone with grayish-green mudstone, containing purplish-red

and brownish-red mudstone in the upper part, and intercalated grayish-black and gray mudstone in the lower part. The K_2n^5 primarily consists of grayish-green and brownish-red mudstone intercalated with grayish-green and grayish-white sandstone and siltstone (Wang et al.,2011; Wu et al.,2014).

65   High-precision U-Pb CA-ID-TIMS (Uranium-Lead Chemical Abrasion-Isotope Dilution-Thermal Ionization Mass Spectrometry) dating of volcanic ash samples from the base of the K_2n^2 interval in borehole SK-1s yielded an age of 83.269 ± 0.044 Ma. This age serves as the chronological anchor for the base of K_2n^2 in borehole G651 (corresponding depth: 1,441 m) through electrofacies correlation of gamma-ray logs (Wu et al.,2013).
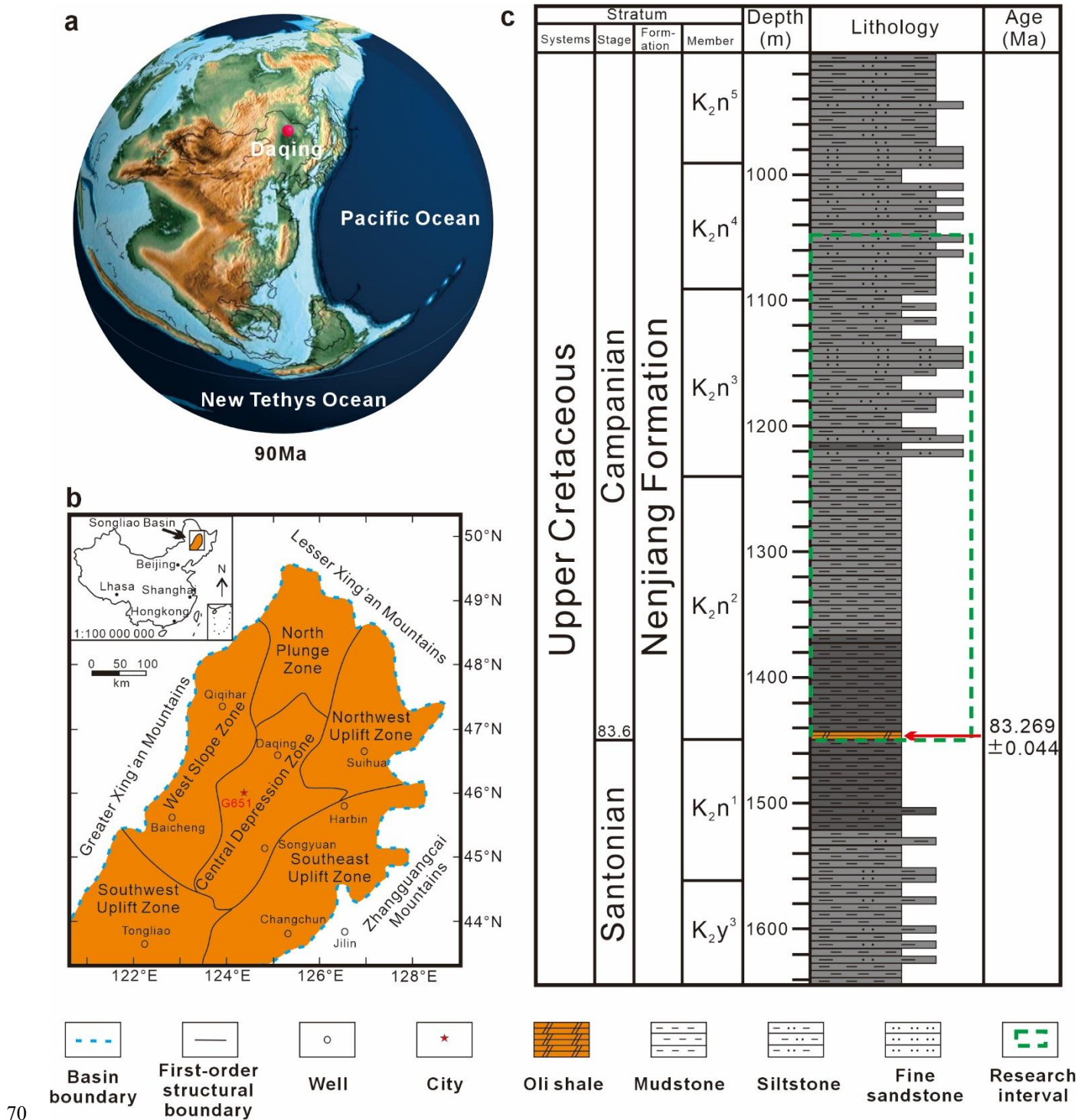
Figure 1: Regional geological map of the study area. (a) Late Cretaceous (90 Ma) paleogeographic map. (b) Tectonic framework of the Songliao Basin and location of borehole G651. (c) Composite stratigraphy of the Nenjiang Formation (K₂n) with isotopic dating horizons.

3 Materials and methods

3.1 Natural Gamma-ray (GR) Logging

Gamma-ray (GR) intensity in stratigraphic sequences primarily reflects concentrations of radioactive isotopes uranium (U), thorium (Th), and potassium (K). Potassium is enriched in clay minerals, feldspars, micas, and evaporites, while U and Th accumulate predominantly in clays, heavy minerals, feldspars, and phosphate minerals. GR logging measures natural gamma-ray emissions from sediments, serving as a sensitive proxy for clay content that records subtle paleoclimatic and paleoenvironmental variations (Baumgarten and Wonik, 2015). Crucially, empirical comparisons of paleoclimate proxies demonstrate that GR data exhibit exceptional sensitivity to Milankovitch orbital forcing while minimizing non-astronomical noise, establishing GR as an optimal indicator for cyclostratigraphy in many depositional settings (Li et al., 2019). Conventionally, low GR values reflect sand-rich lithofacies, while high GR values characterize mudstones, oil shales, and other fine-grained deposits.

This study utilizes GR logging data from the K_2n^{2-3} of the Cretaceous Nenjiang Formation in borehole G651, drilled in the central Gulong Sag of the Songliao Basin. The dataset features a sampling resolution of 0.0508 m (0.2 in) across depths of 1,050-1,450 m.

3.2 Time-Series methods

In this study, the long-term trend of gamma-ray (GR) data was removed by subtracting the 35% (i.e., 140m) locally weighted scatterplot smoothing (LOESS) trend, as recommended by Cleveland and Devlin (1988). Following preprocessing (outlier elimination and resampling to equidistant intervals), detrended GR data underwent spectral analysis via the multitaper method (MTM; Thomson, 1982). Significant periodic components were identified by testing MTM power spectra against a robust first-order autoregressive [AR (1)] noise model at the 95% confidence level (Mann and Lees, 1996).

Time-optimal sedimentation rates were determined using the correlation coefficient (COCO) method, which assumes constant sedimentation rates within the target interval. Variable sedimentation rates were identified using the evolutionary correlation coefficient (eCOCO) method (Li et al., 2018). These methods provide critical constraints for reconstructing paleoenvironmental evolution and validating temporal completeness.

Depth-to-time conversion was implemented using derived orbital tuning targets, establishing a high-resolution floating time scale. All analyses employed Acycle v2.8 software (Li et al., 2019), ensuring reproducibility.

3.3 Palynology

Palynological examination of 17 samples from borehole G651 in the central Gulong Sag identified 57 fossil taxa spanning 36 genera. The results of pollen analysis are from the State Key Laboratory of Petroleum Resources and Engineering in China

University of Petroleum,Beijing.Sample processing employed standardized acid-digestion protocols: mechanical
disaggregation followed by sequential chemical treatment with 30% hydrochloric acid (HCl) to dissolve carbonates and 40%
hydrofluoric acid (HF) for silicate removal, with subsequent filtration through 10-μm nylon mesh using ultrasonic agitation,
centrifugation at 3,000 rpm for 5 minutes, and permanent slide preparation for transmitted-light microscopic analysis.

4 Results

4.1 Time-Series Analysis

By comparing the ratios of the dominant peaks in the power spectrum analysis (Figure 2a) with the ratios of the Earth's
orbital parameters from the Late Cretaceous (Figure 2b), we identified an astronomical forcing signal in the gamma-ray (GR)
log data. Based on the La2004 and La2010 astronomical solutions, we obtained the theoretical periods for the 80-84 Ma
interval (Laskar et al., 2004; Laskar et al., 2011). As shown in Figure 3c, the Late Cretaceous Earth's orbital parameters were:
405 kyr (E: eccentricity), 125 kyr (e1: eccentricity), 95 kyr (e2: eccentricity), 38.5 kyr (O: obliquity), 22.8 kyr (P1:
precession), 21.5 kyr (P2: precession), and 18.5 kyr (P3: precession). The 2π Multi-Taper Method (MTM) power spectrum
of the detrended GR series from the K_2n^{2-3} interval of well G651 (Figure 2b) shows significant peaks (>99% confidence level)
at wavelengths of 46.51 m, 18.02 m, 12.20 m, 4.64 m, 2.90 m, and 2.32 m. By comparing the two, it can be tentatively
inferred that the 46.51 m cycle corresponds to the 405 kyr (E) cycle, the 12.20 m cycle corresponds to the 95 kyr (e2) cycle,
the 4.64 m cycle corresponds to the 38.5 kyr (O) cycle, the 2.90 m cycle corresponds to the 22.8 kyr (P1) cycle, and the 2.32
m cycle corresponds to the 18.5 kyr (P3) cycle. However, these correlations still require further verification through analysis
of the sedimentation rate. The evolutionary FFT power spectrum reflects vertical changes in the sedimentation rate (Figure
2c).

These correlations require verification through sedimentation rate optimization, as the evolutionary FFT spectrum (Figure 2c)
indicates significant vertical sedimentation rate variations.
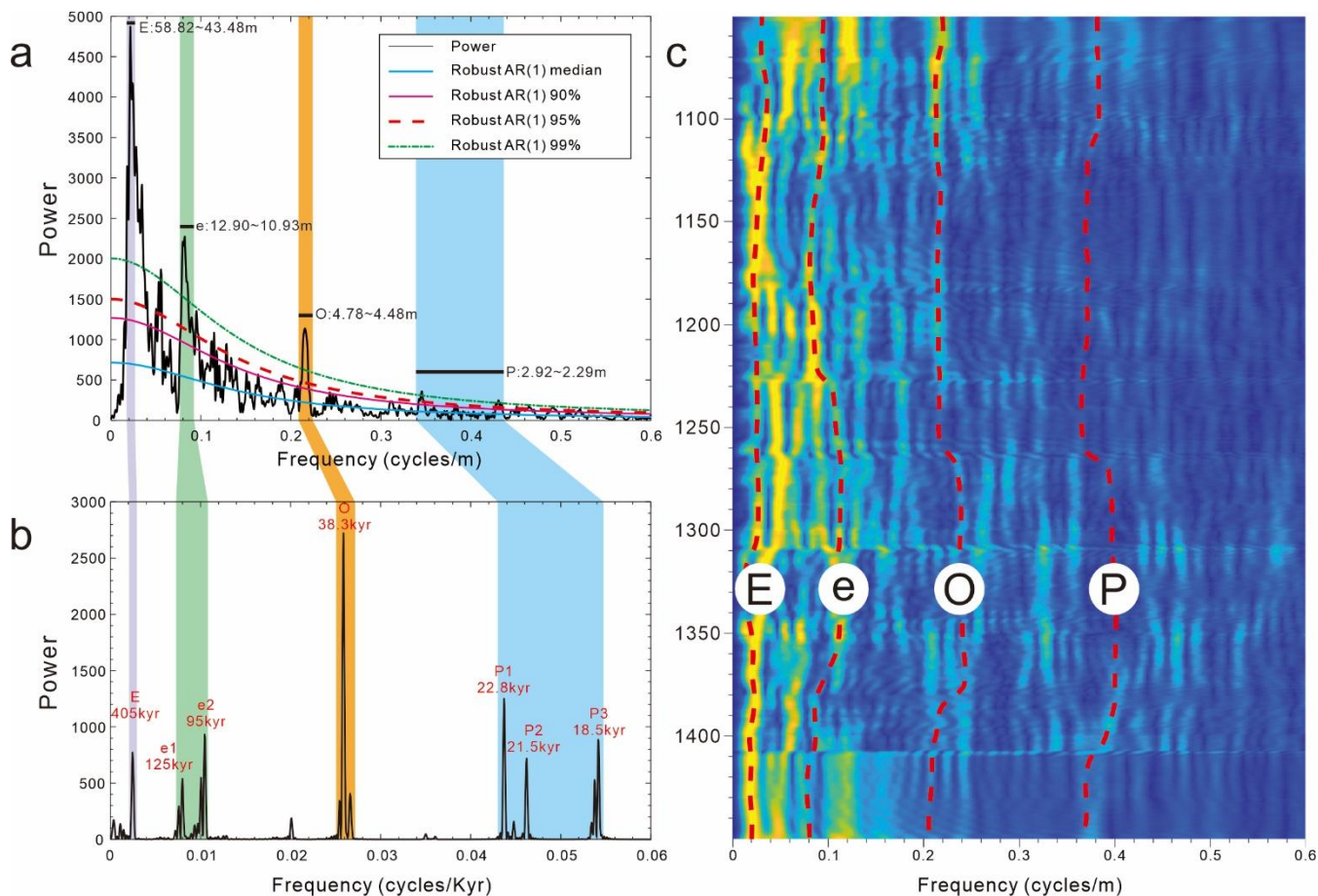
Figure 2: (a) Power spectrum of the gamma-ray (GR) series for the K₂n²⁻³ in borehole G651. (b) Spectral plot of the eccentricity-tilt-precession (ETP) parameters for 80–84 Ma. (c) Evolutionary FFT spectrogram with an 80-m sliding window.

Wu et al. (2014) reported an average sedimentation rate of 13.99 cm/kyr for the K_2n^{2-3} in borehole SK-1n. To determine the optimal sedimentation rate, a COCO analysis with 5000 Monte Carlo simulations was conducted for sedimentation rates ranging from 0 to 20 cm/kyr, using a sliding window length of 100m (within the estimated range of 150~200% of the 405 kyr sedimentation thickness). As shown in Figure 3a, the COCO sedimentation rate plot for the detrended GR series exhibits a peak correlation coefficient at 12.1 cm/kyr. This result demonstrates statistical significance exceeding the 99.9% confidence level ($p < 0.001$) against the null hypothesis (H_0) (Figure 3b) and aligns with all seven theoretically predicted orbital parameters contributing to the signal (Figure 3c).

Evolutionary COCO (eCOCO) analysis (Li et al., 2018) resolves significant sedimentation rate variations with pronounced peaks in the 7–14 cm/kyr range (Figure 3g), exhibiting high correlation coefficients ($\rho > 0.85$), null hypothesis (H_0) rejection exceeding 99.9% confidence ($p < 0.001$), and alignment with all seven theoretical orbital parameters (Figure 3d-f), thereby corroborating conventional COCO results; consequently, astronomical tuning assigns depth intervals as follows: 58.82–

43.48 m to 405kyr long eccentricity, 12.90–10.93 m to 95kyr short eccentricity, 4.78–4.48 m to 38.3kyr obliquity, and 2.92–2.29 m to 22.8–18.5kyr precession bands (Figure 2a).
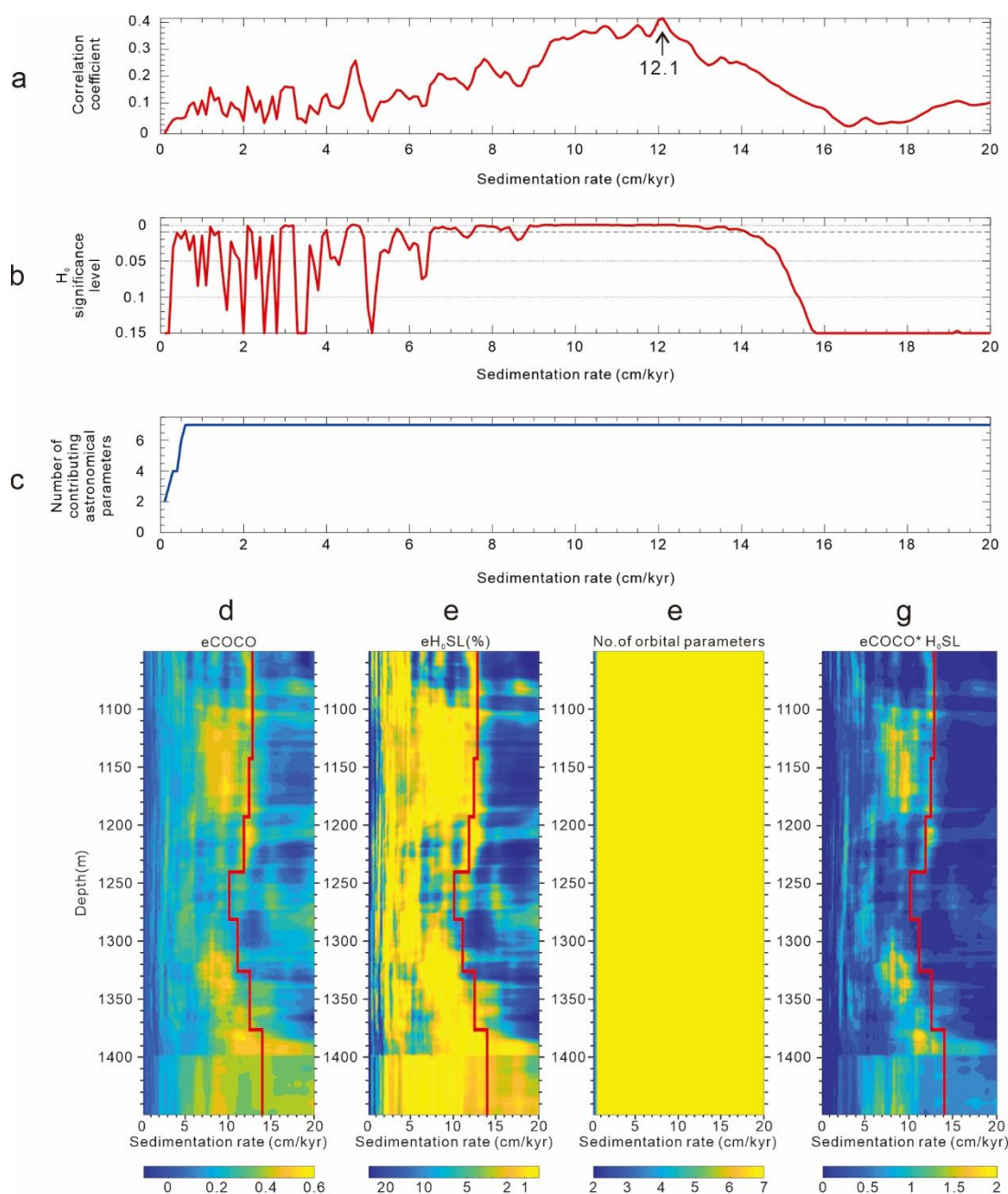
Figure 3: Cyclostratigraphic analyses of the detrended GR series. (a) Correlation coefficient plot from COCO analysis. (b) Null hypothesis (H₀) significance level plot for COCO analysis. (c) Time-series variation in the number of contributing astronomical parameters for COCO analysis. (d) Correlation coefficient plot from eCOCO analysis. (e) Null hypothesis (H₀) significance level

plot for eCOCO analysis. (f) Depth-varying number of contributing astronomical parameters for eCOCO analysis. (g) Composite sedimentation rate spectrogram from eCOCO analysis.

150

4.2 Astronomically Calibrated Timescale

A series of filtering results were obtained by applying the Taner-Hilbert filtering method to the detrended GR data. Among them, the 405 kyr long eccentricity result was obtained within the bandwidth range of 0.017–0.023 cycle/m, the 95 kyr short eccentricity result within 0.078–0.092 cycle/m, the 38.3 kyr obliquity result within 0.209–0.223 cycle/m, and the 22.8 kyr

155   precession result within 0.342–0.349 cycle/m. A total of 8 cycles of 405 kyr, 34 cycles of 95 kyr, 86 cycles of 38.3 kyr, and 138 cycles of 22.8 kyr were identified. The 405 kyr long eccentricity cycle was used to tune the filtering results of 0.017–0.023 cycle/m, yielding a floating astronomical time scale for K_2n^{2-3}. Using the volcanic ash age (83.269 ± 0.044 Ma) at the base of K_2n^2 as an anchor point (He et al., 2012; Wang et al., 2016), the absolute astronomical time scale for K_2n^{2-3} was established (Figure 4).

160

10.5194/egusphere-2025-5799
2025-12-18
EGUsphere
Author(s) 2025. CC BY 4.0 License.
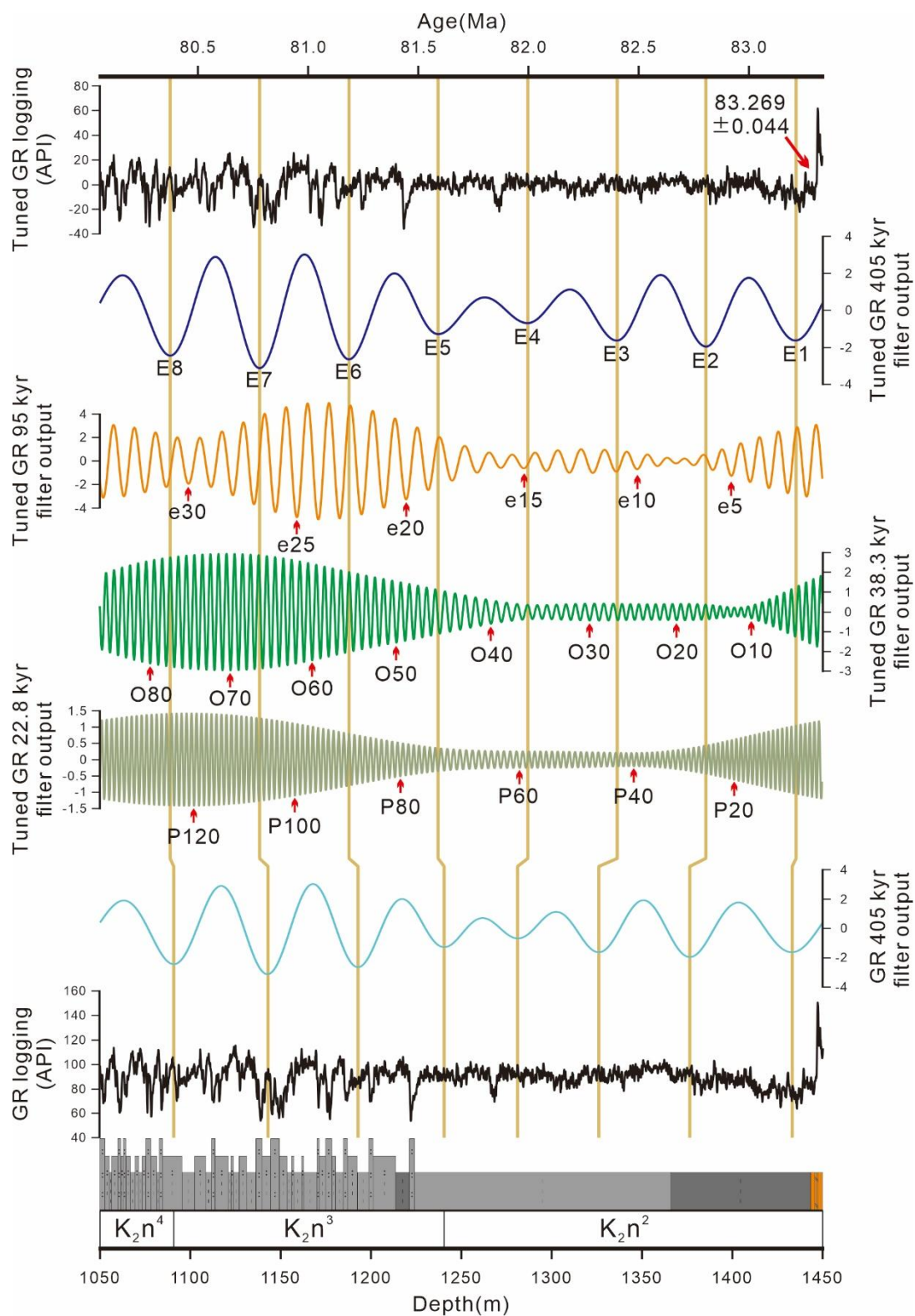
Figure 4: Astronomically tuned timescale for the K_2n^{2-3} in borehole G651.

4.3 Palynological Characteristics

165 Seventeen palynological samples were collected at 0.5m intervals from the lower K_2n^3 (1210.89–1218.89 m) in borehole G651, with microscopic analysis identifying 57 taxa representing 36 genera; pteridophyte spores (12 genera, 23 species) comprised 22.34–41.12% (mean 33.95%) of the total assemblage, dominated by *Deltoidospora* (9.52–17.54%; mean 12.92%)(Figure 5a), followed by *Cyathidites* (5.62–17.73%; mean 10.00%)(Figure 5b), *Cicatricosisporites* (1.97–11.64%; mean 7.08%)(Figure 5c), and *Impardecispora* (0.44–3.95%; mean 1.71%)(Figure 5d), while all other genera each constituted
170 <1% (mean) with discontinuous occurrence across samples (Table 1).

Table 1: Quantitative summary of pteridophyte spore taxa

num	depth	*Dictyotriletes*	*Neoraistrickia*	*Cyathidites*	*Osmundacidites*	*Cicatricosisporites*	*Impardecispora*	*Klukisporites*	*Pilosisporites*	*Lycopodiacidities*	*Deltoidospora*	*Foveotriletes*	*Buttinia*	**Pteridophytes**
BF-38	1210.89			14		7	1				18	2		**42**
BF-37	1211.39			16	2	12	6	1			20	1		**58**
BF-36	1211.89			16	3	6	5				24	5		**59**
BF-35	1212.39			10	1	14	4		1		18	1		**49**
BF-34	1212.89			26	1	12	5				27			**71**
BF-33	1213.39			18	1	16	2				20			**57**
BF-32	1213.89			23	2	24	1				40	1		**91**
BF-31	1214.39			8		13	4				19	1		**45**
BF-30	1214.89			50		17	2				38	2		**109**
BF-29	1215.39	1		16	2	22	3				18	1	1	**64**
BF-28	1215.88			36	1	18	2			1	27	2	1	**88**
BF-27	1216.39			16	2	14	5			2	21	6	1	**67**
BF-26	1216.89			28	5	22	4				34	2		**95**
BF-25	1217.39			20	2	15	1			2	27	1		**68**
BF-24	1217.89		1	21		18	1				33	4		**78**
BF-23	1218.39			10	1	6	6			3	23	1		**50**
BF-22	1218.89	2		18	1	3	1		1	1	25	1		**53**

Gymnosperm pollen (14 genera, 21 species) constituted 55.07–75.00% (mean 61.49%) of the total palynoflora, with

175   *Classopollis* ranking first in abundance (2.21–22.43%; mean 14.38%)(Figure 5e), *Pinuspollenites* second (7.89–18.23%; mean 11.34%)(Figure 5f), *Ephedripites* third (2.66–13.37%; mean 8.05%)(Figure 5g), *Cycadopites* fourth (1.97–11.70%; mean 7.44%)(Figure 5h), *Podocarpidites* fifth (1.60–14.92%; mean 5.64%)(Figure 5i), *Perinopollenites* sixth (0.55–9.21%; mean 3.45%)(Figure 5j), *Taxodiaceaepollenites* seventh (0.00–6.42%; mean 2.68%)(Figure 5k), *Tsugaepollenites* eighth (0.79–5.85%; mean 2.64%)(Figure 5l), *Chasmatosporites* ninth (0.47–7.24%; mean 2.61%)(Figure 5m), and *Parvisaccites*

180   tenth (0.73–4.23%; mean 1.81%)(Figure 5n), while all other genera each constituted <1% (mean) (Table 2).

Table 2: Quantitative summary of gymnosperm pollen taxa

num	depth	*Parvisaccites*	*Podocarpidites*	*Classopollis*	*Exesipollenites*	*Perinopollenites*	*Taxodiaceaepollenites*	*Chasmatosporites*	*Ephedripites*	*Cedripites*	*Jiaohepollis*	*Pinuspollenites*	*Tsugaepollenites*	*Cycadopites*	*Jugella*	**Gymnospermae**
BF-38	1210.89	7	22	21		10	8	5	5	1		29	11	22		**141**
BF-37	1211.39	2	11	7		14	3	11	7	1		25	5	3		**89**
BF-36	1211.89	3	27	4		1	6	3	20	1	1	33	4	10	1	**114**
BF-35	1212.39	2	7	18	4	4	4	8	16			17	8	8	1	**97**
BF-34	1212.89	2	3	28		7	12	1	25	1	1	15	4	11	2	**112**
BF-33	1213.39	3	7	38	1	2	12	5	20	1	1	23	6	19	1	**139**
BF-32	1213.89	3	6	47		4	13	2	12	1	1	18	6	17	1	**131**
BF-31	1214.39	1	5	23		6	5	3	10			15	2	10		**80**
BF-30	1214.89	6	17	43		6		2	35		1	25	8	16	2	**161**
BF-29	1215.39	8	6	28	2	7	2	3	19	1		16	4	20	2	**118**
BF-28	1215.88	3	7	48		5		1	15			17	2	22		**120**
BF-27	1216.39	2	14	42		7	9	5	19			24	6	17	1	**146**
BF-26	1216.89	3	16	45	2	7		4	10		1	26	2	24		**140**
BF-25	1217.39	6	15	29		8	6	11	21	1		28	6	15	1	**147**
BF-24	1217.89	3	17	18	4	13	1	6	11		2	22	4	11	2	**114**
BF-23	1218.39	4	7	26		5	6	8	18	1		21	3	16	2	**117**
BF-22	1218.89	3	3	27		5		4	8	2		18	5	11		**86**

Angiosperm pollen (10 genera, 13 species) comprised 2.14–8.55% (mean 4.56%) of the total palynoflora, with
185 *Aquilapollenites* being predominant (0.00–2.94%; mean 1.31%)(Figure 5o), *Complexiopollis* the second most abundant
(0.00–1.97%; mean 0.88%)(Figure 5p), and *Callistopollenites* the third (0.00–2.25%; mean 0.78%)(Figure 5q), while all
other genera individually constituted <0.50% (mean) (Table 3).

Table 3: Quantitative summary of angiosperm pollen taxa

num	depth	*Areciotes*	*Borealipollis*	*Myricipites*	*Lythraites*	*Beaupreaidites*	*Proteacidies*	*Translucentipollis*	*Aquilapollenites*	*Callistopollenites*	*Complexiopollis*	**Angiospermae**
BF-38	1210.89			2					3			**5**
BF-37	1211.39				1				2	1	1	**5**
BF-36	1211.89	2		1		1			2	1	1	**8**
BF-35	1212.39				1	1			2		1	**5**
BF-34	1212.89					1			1		2	**4**
BF-33	1213.39		1					1	2	4	1	**9**
BF-32	1213.89	3							1	1	1	**6**
BF-31	1214.39	4	1					1	4		1	**11**
BF-30	1214.89	2	1			2	1	1	3		2	**12**
BF-29	1215.39		1					1	3	1	1	**7**
BF-28	1215.88		1	2	1					1	1	**6**
BF-27	1216.39		1						2	1	1	**5**
BF-26	1216.89		3			2		2	5	2	3	**17**
BF-25	1217.39		1						3	4	3	**11**
BF-24	1217.89	2	2			1			3	3	4	**15**
BF-23	1218.39						1	1	2	4	3	**11**
BF-22	1218.89		2	1					4	3	3	**13**

190
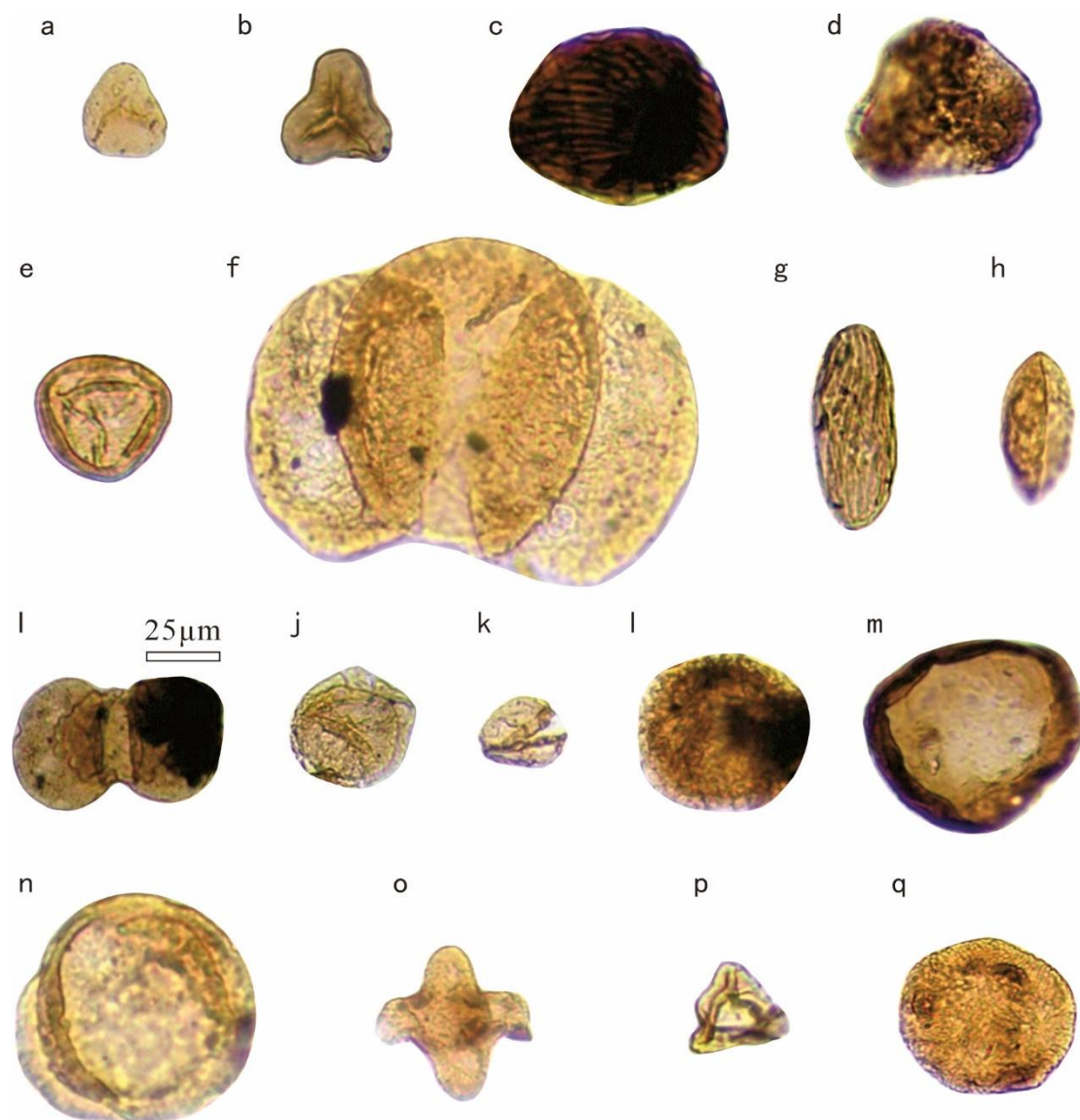
Figure 5: Typical palynomorphs from K₂n³. **a.** *Deltoidospora*; **b.** *Cyathidites*; **c.** *Cicatricosisporites*; **d.** *Impardecispora*; **e.** *Classopollis*; **f.** *Pinuspollenites*; **g.** *Ephedripites*; **h.** *Cycadopites*; **i.** *Podocarpidites*; **j.** *Perinopollenites*; **k.** *Taxodiaceaepollenites*; **l.** *Tsugaepollenites*; **m.** *Chasmatosporites*; **n.** *Parvisaccites*; **o.** *Aquilapollenites*; **p.** *Complexiopollis*; **q.** *Callistopollenites*.

195

5. Discussion

5.1 Astronomical Timescale for the K_2n^{2-3} Interval in the Gulong Area

Current zircon ages from volcanic ash layers in the Songliao Basin are predominantly constrained within the lower Nenjiang Formation (K_2n), lower Qingshankou Formation(K_2qn), and lower Yingcheng Formation(K_1yc) (Wu et al., 2024), with

200   chronostratigraphic benchmarks including U-Pb SIMS dating of volcanic ash at the base of K_2n^2 in borehole SK-1s yielding 83.7 ± 0.5 Ma (He et al., 2012), reanalysis of the same sample via high-precision U-Pb CA-ID-TIMS producing 83.269 ± 0.044 Ma (Wang et al., 2016), and U-Pb SIMS dating of ash proximal to the K_2n^2 boundary in borehole SK-2 providing 83.3 ± 0.6 Ma (Yu et al., 2019).

The concentration of absolute ages within the first and second members of the Nenjiang Formation, coupled with continuous

205   sedimentation and the absence of identifiable unconformities from K_2n^2 to K_2n^5, challenges precise age determination for the K_2n^3–K_2n^5 (Wu et al., 2024).

Wu et al. (2014) derived an age range of 82.392–83.823 Ma (duration: 1.431 Myr) for the K_2n^2 and 81.595–82.392 Ma (duration: 0.797 Myr) for the K_2n^3 in borehole SK-1n through cyclostratigraphic analysis of thorium (Th) spectral logging data. Subsequently, Ma et al. (2020) obtained ages of 81.02–83.28 Ma (duration: 2.26 Myr) for K_2n^2 and 79.68–81.02 Ma

210   (duration: 1.34 Myr) for K_2n^3 in borehole SK-2 using similar methods.

This study utilizes the highest-precision zircon age of 83.269 ± 0.044 Ma to define the base of the K_2n^2. Comparative analysis of the 2π MTM power spectrum and COCO-derived sedimentation rates (Figure 2a vs. Figure 3a) confirms methodological consistency, while evolutionary spectral analysis and eCOCO sedimentation rate profiles both exhibit higher sedimentation rates at both boundaries than in the mid-interval (Figure 2c and Figure 3d-g), with the red curve in Figure 3g

215   representing the sedimentation rate tuned to 405-kyr eccentricity cycles, ultimately determining K_2n^2 at 1240.54–1450.00 m (thickness 209.46 m) spanning 81.591–83.333 Ma (duration 1.742 Myr), and K_2n^3 at 1090.78–1240.54 m (thickness 149.76 m) spanning 80.376–81.591 Ma (duration 1.215 Myr).

The floating astronomical timescale established in this study exhibits discrepancies with previous works: while the K_2n^2 age model aligns closely with Wu et al. (2014), significant divergence occurs in K_2n^3, primarily attributable to the identification

220   of three 405kyr cycles within K_2n^3 in this study versus approximately two cycles in Wu et al. (2014), despite minimal differences in sedimentation rates between the two models. Conversely, substantial disparities in sedimentation rates between this study and Ma et al. (2020) result in low similarity between their respective age models.

Future acquisition of new zircon ages from volcanic ashes within the K_2n^2-K_2n^5 will be essential to resolve current controversies regarding stratigraphic ages across the basin.

225   ### 5.2 Palynostratigraphic Age Assignment

Within the K_2n^3, palynomorphs including *Pinuspollenites*, *Cyathidites*, *Podocarpidites*, *Exesipollenites*, *Cicatricosisporites*, *Classopollis*, *Foveotriletes*, and *Parvisaccites* represent characteristic Cretaceous taxa (Tian et al., 2005; Xu et al., 2021; Gao

et al., 2023). Gao et al. (1999) established two palynological assemblages for the Nenjiang Formation: the lower K_2n^1 features a *Proteacidites-Cyathidites-Dictyotriletes* assemblage, while the upper K_2n^2-K_2n^5 are characterized by the

230 *Lythraites-Aquilapollenites-Schizaeoisporites* assemblage. Crucially, *Lythraites* first appears in K_2n^2, whereas *Aquilapollenites* serves as a diagnostic taxon for K_2n^2-K_2n^5 (Wan et al., 2013). This genus exhibits cosmopolitan distribution with peak abundance during the Late Cretaceous, particularly the Campanian to Maastrichtian stages.

Collectively, the palynomorph assemblage from the K_2n^3 in the study area indicates a Late Cretaceous Campanian age.

5.3 Palynological Characteristics and Paleoclimate Reconstruction

235 Based on ecological attributes of parent plants, the palynoflora was classified into five categories: coniferous plants, shrubby plants, evergreen broad-leaved plants, herbaceous plants, and deciduous broad-leaved plants. Note that no definitive deciduous broad-leaved types were identified in the K_2n^3 of borehole G651.

Using modern thermal zonation as an analog, Cretaceous palynomorphs in the Songliao Basin were grouped into five climatic types: tropics, tropics-subtropics, tropics-temperate, subtropics, and tropics-temperate plants. For moisture

240 preferences, we adopted Jing et al. (2011)'s classification: xerophytic, mesophytic, helophytic, hygrophytic, and hydrophytic taxa, with an absence of true hydrophytes in the study area (Table 4).

Within the vegetation classification (Figure 6), coniferous taxa predominated (28.88–48.40%; mean 36.78%), followed by shrubby taxa as the second most abundant (8.51–25.40%; mean 18.78%), evergreen broad-leaved taxa ranked third (11.92–26.98%; mean 17.43%), while herbaceous taxa constituted the smallest proportion (10.24–18.86%; mean 14.64%).

245 In the climatic belt classification (Figure 6), tropics taxa predominated (23.68–39.53%; mean 32.21%), followed by tropics-subtropics taxa as the second most abundant (16.57–38.60%; mean 28.91%), tropics-temperate taxa ranked third (9.63–24.31%; mean 14.78%), while subtropics taxa constituted a quantitatively minor component (0.93–7.95%; mean 3.40%) and temperate taxa represented the smallest proportion (2.66–13.90%; mean 8.26%).

Within the moisture preference classification (Figure 6), hygrophytic taxa predominated (30.90–46.10%; mean 39.22%),

250 followed by mesophytic taxa as the secondary dominant (15.51–32.45%; mean 21.86%), xerophytic taxa ranked third (9.87–30.24%; mean 23.20%), while helophytic taxa constituted a negligible component (0.00–3.31%; mean 1.12%).

Synthesizing the evidence, the palynomorph assemblage from the lower K_2n^3 in borehole G651 indicates a warm-humid paleoclimate characterized by seasonal moisture variability.

255

260

Table 4: Classification of palynomorph-derived vegetation types, climatic belts, and moisture preference classes

Spores and pollen	Vegetation type	Climate type	Humidity type
Neoraistrickia	herb	-	-
Cyathidites	evergreen broad-leaf forest	tropics	humidogene
Osmundacidites	herb	tropics-temperate	helophyte
Cicatricosisporites	shrub	tropics	humidogene
Impardecispora	shrub	tropics	humidogene
Klukisporites	shrub	tropics	humidogene
Pilosisporites	shrub	-	humidogene
Deltoidospora	herb	tropics-subtropics	humidogene
Foveotriletes	herb	tropics-temperate	mesophyte
Parvisaccites	coniferous forest	tropics-temperate	mesophyte
Podocarpidites	coniferous forest	tropics	humidogene
Classopollis	coniferous forest	tropics-subtropics	xerophyte
Exesipollenites	coniferous forest	subtropics	helophyte
Taxodiaceaepollenites	coniferous forest	subtropics	helophyte
Ephedripites	shrub	temperate	xerophyte
Cedripites	coniferous forest	subtropics	mesophyte
Jiaohepollis	coniferous forest	temperate	-
Pinuspollenites	coniferous forest	tropics-temperate	mesophyte
Tsugaepollenites	coniferous forest	subtropics	-
Cycadopites	-	tropics	mesophyte
Lythraites	herb	-	-
Beaupreaidites	shrub	tropics	humidogene
Proteacidites	shrub	tropics	humidogene
Cranwellia	shrub	-	-
Translucentipollis	shrub	tropics-subtropics	humidogene
Aquilapollenites	shrub	tropics-subtropics	humidogene
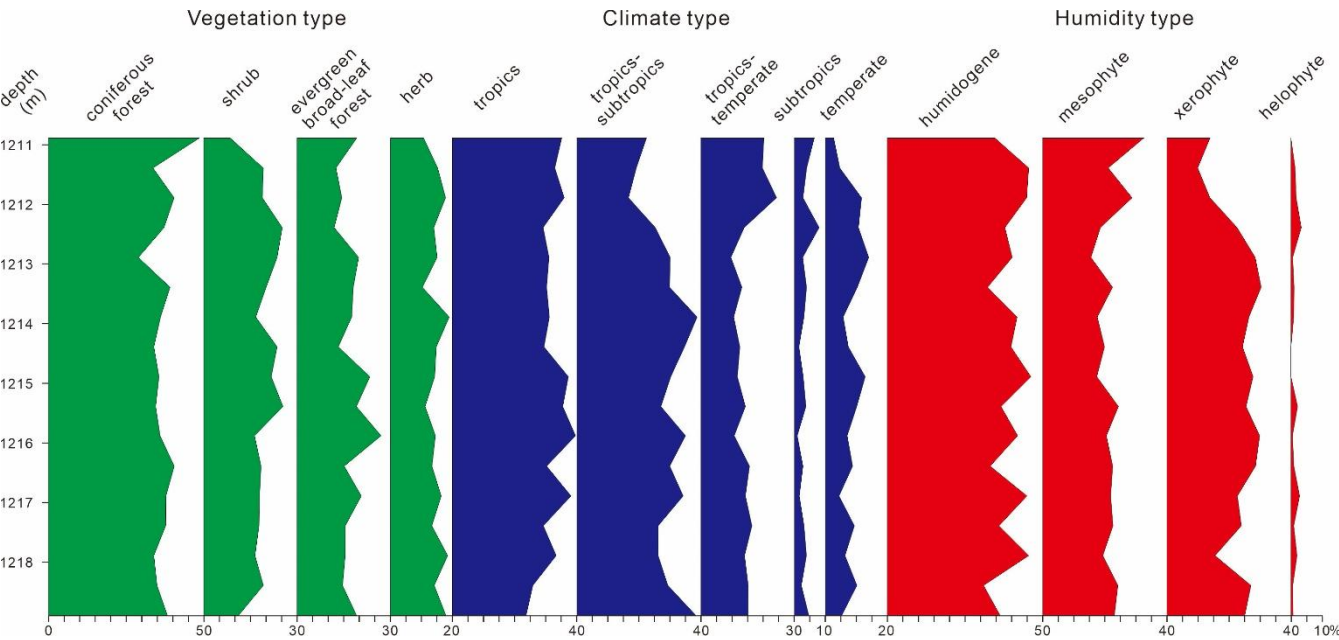
Figure 6: Palynomorph-derived vegetation types, climatic belts, and moisture preference classes with quantitative distributions.

265

5.4 Astronomically Paced Climate Periodicity

Spectral comparison between palynomorph-defined climatic belt preferences and astronomically filtered cycles reveals distinct periodic fluctuations in the two dominant types: tropics taxa exhibit variation patterns synchronous with the 38.3kyr obliquity filter output, while tropics-subtropics taxa display an opposite phase relationship to obliquity forcing (Figure 7).

270 The slope affects the latitudinal distribution of solar radiation by adjusting the Earth's axial tilt. By comparing the La2004 slope with the annual solar radiation distribution at 45° N (close to the latitude of the Songliao Basin during the Cretaceous period) (Laskar et al., 2004), it was found that both exhibit similar variation cycles. Shi et al. (2011) proposed that the East Asian summer monsoon is primarily influenced by the precession cycle (approximately 20,000 years), while the winter monsoon is mainly driven by the obliquity cycle (around 40,000 years). The obliquity forcing affects the evolution of the

275 East Asian winter monsoon by modulating the meridional difference in solar radiation. When the slope is higher, mid-latitude regions receive more annual solar radiation, resulting in warm and humid climates, higher populations of tropical climate-type plant species, and lower populations of tropical-subtropical climate-type plant species. During this period, lake water bodies expand, muddy sediments develop, and the GR readings in well logs are higher. Conversely, when the slope is lower, mid-latitude regions receive less annual solar radiation, leading to cold and dry climates, lower populations of tropical

280 climate-type plant species, and higher populations of tropical-subtropical climate-type plant species. During this period, lake water bodies contract, muddy sediments decrease, and the GR readings in well logs are lower.

Due to the relatively thin stratigraphic thickness covered by the palynological data in this study, it is not possible to determine the controlling effect of longer-term climate changes on sedimentary cycles. Further verification with better data is needed in the future.

285
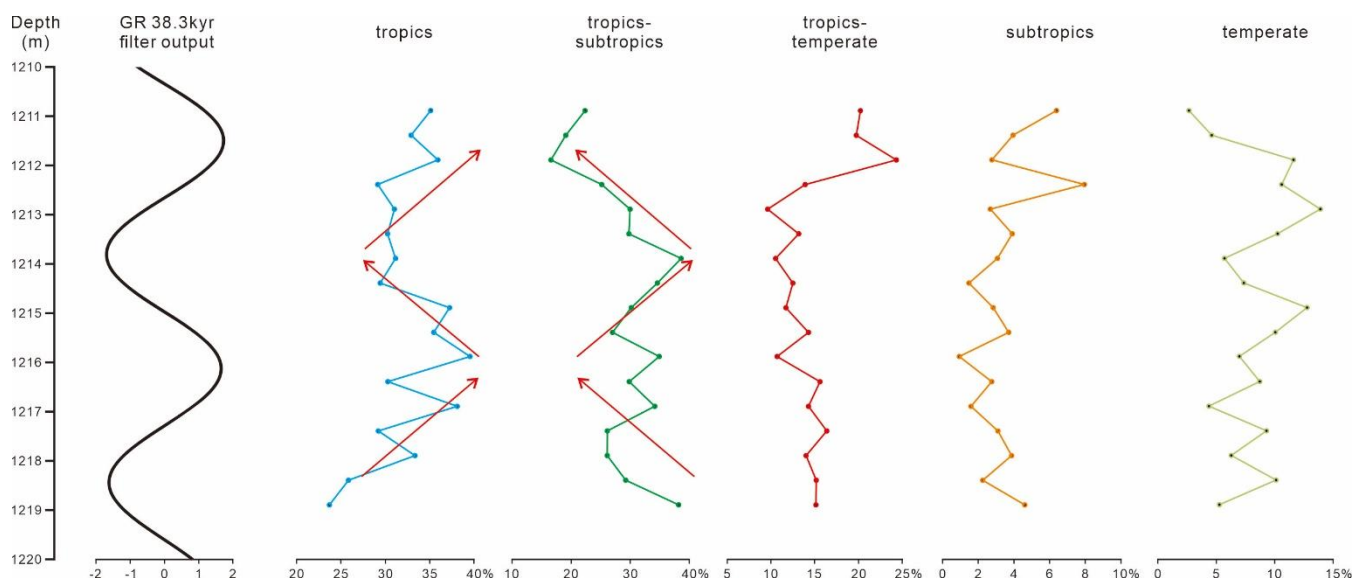
Figure 7: Orbital-scale cyclicity in palynomorph-derived climatic belt preferences and its phase relationship with obliquity forcing

6. Conclusions

290 Cyclostratigraphic analysis of gamma-ray (GR) logging data from borehole G651 confirms prominent ~405kyr long eccentricity, ~95kyr short eccentricity, ~38.3kyr obliquity, and 22.8kyr precession cycles within the central Songliao Basin's K_2n^{2-3}, demonstrating astronomical forcing on its deposition. Construction of a floating astronomical time scale (FATS) via GR tuning, anchored by high-precision volcanic ash zircon ages, yields the following key results:

(1) The K_2n^2 spans 1240.54–1450.00 m (thickness: 209.46 m), corresponding to 81.591–83.333 Ma (duration: 1.742 Myr).

295 The K_2n^3 extends from 1090.78–1240.54 m (thickness: 149.76 m), spanning 80.376–81.591 Ma (duration: 1.215 Myr).

(2) Palynomorphs at the K_2n^3 base indicate a Late Cretaceous Campanian age and reconstruct a warm-humid paleoclimate.

(3) Integration of cyclostratigraphic and palynological data reveals obliquity forcing (38.3-kyr cycles) as the primary driver of cyclic climate shifts at the K_2n^3 base.

300 **Author contribution**

YG, JH, and SG planned the campaign; YG performed the measurements; YG analyzed the data; YG wrote the manuscript draft; JH and SG reviewed and edited the manuscript.

Competing interests

The authors declare that they have no conflict of interest.

305 **Acknowledgements**

We would like to thank anonymous reviewers for their suggestions.

References

Baumgarten, H. and Wonik, T.: Cyclostratigraphic studies of sediments from Lake Van (Turkey) based on their uranium contents obtained from downhole logging and paleoclimatic implications, International Journal of Earth Sciences, 104,
310 1639–1654, 10.1007/s00531-014-1082-x, 2014.

Cleveland, W. S. and Devlin, S. J.: Locally Weighted Regression: An Approach to Regression Analysis by Local Fitting, Journal of the American Statistical Association, 83, 596–610, https://doi.org/10.1080/01621459.1988.10478639, 1988.

Feng, Z., Jia, C., Xie, X., Zhang, S., Feng, Z., and Cross, T. A.: Tectonostratigraphic units and stratigraphic sequences of the nonmarine Songliao basin, northeast China, Basin Research, 22, 79–95, 10.1111/j.1365-2117.2009. 00445.x, 2010.

315 Gao, R., Zhao, C., and Qiao, X.: Cretaceous Oil Strata Palynology from Songliao Basin, Geological Publishing House, Beijing1999.

Gao, Y., Qin, T., Li, R., Zhou, Y., Liu, H., Li, M., Zhu, C., and Liu, W.: Palynological Records and Paleoclimatic Characteristics of Nenjiang Formation in Lishu Fault Depression,Songliao Basin, Journal of Jilin University (Earth Science Edition), 53, 1391–1402, 10.13278/j.cnki.jjuese.20220130, 2023.

320 Hays, J. D., Imbrie, J., and Shackleton, N. J.: Variations in the Earth's Orbit: Pacemaker of the Ice Ages, Science, 194, 1121–1132, 10.1126/science.194.4270.1121, 1976.

He, H. Y., Deng, C. L., Wang, P. J., Pan, Y. X., and Zhu, R. X.: Toward age determination of the termination of the Cretaceous Normal Superchron, Geochem Geophy Geosy, 13, Artn Q02002
10.1029/2011gc003901, 2012.

325 Hinnov, L. A.: Cyclostratigraphy and its revolutionizing applications in the earth and planetary sciences, Geological Society of America Bulletin, 125, 1703–1734, 10.1130/b30934.1, 2013.

Jing, X., Li, S., Xi, D., and Wan, X.: Late Cretaceous spores and pollen assemblages and paleoclimate record of the Nenjiang Formation in Nong'an, Jilin province, Acta Micropalaeontologica Sinica, 28, 193–203, 2011.

330   Laskar, J., Fienga, A., Gastineau, M., and Manche, H.: La2010: a new orbital solution for the long-term motion of the Earth, Astronomy & Astrophysics, 532, 10.1051/0004-6361/201116836, 2011.

Laskar, J., Robutel, P., Joutel, F., Gastineau, M., Correia, A. C. M., and Levrard, B.: A long-term numerical solution for the insolation quantities of the Earth, Astronomy & Astrophysics, 428, 261–285, 10.1051/0004-6361:20041335, 2004.

Li, M., Hinnov, L., and Kump, L.: Acycle: Time-series analysis software for paleoclimate research and education, Computers & Geosciences, 127, 12–22, 10.1016/j.cageo.2019.02.011, 2019.

335   Li, M., Kump, L. R., Hinnov, L. A., and Mann, M. E.: Tracking variable sedimentation rates and astronomical forcing in Phanerozoic paleoclimate proxy series with evolutionary correlation coefficients and hypothesis testing, Earth and Planetary Science Letters, 501, 165–179, 10.1016/j.epsl.2018.08.041, 2018.

Li, X., Huang, Y., Zhang, Z., and Wang, C.: Chemical weathering characteristics of the Late Cretaceous Nenjiang Formation from the Songliao Basin (Northeastern China) reveal prominent Milankovitch band variations, Palaeogeography,
340   Palaeoclimatology, Palaeoecology, 601, 10.1016/j.palaeo.2022.111130, 2022.

Li, Z., Chen, J., Zou, H., Wang, C., Meng, Q. a., Liu, H., and Wang, S.: Mesozoic–Cenozoic tectonic evolution and dynamics of the Songliao Basin, NE Asia: Implications for the closure of the Paleo-Asian Ocean and Mongol-Okhotsk Ocean and subduction of the Paleo-Pacific Ocean, Earth-Science Reviews, 218, 10.1016/j.earscirev.2020.103471, 2021.

Ma, X., Wu, H., Fang, Q., Shi, M., and Zhang, S.: A Floating Astronomical Time Scale for the Early Late Cretaceous
345   Continental Strata in the Songliao Basin, Northeastern China, Acta Geologica Sinica (English Edition), 94, 27–37, 10.1111/1755-6724.14497, 2020.

Mann, M. E. and Lees, J. M.: Robust estimation of background noise and signal detection in climatic time series, Climatic Change, 33, 409–445, 10.1007/bf00142586, 1996.

Milankovitch, M.: Kanon der Erdbestrahlung und seineAndwendung auf das Eiszeitenproblem, Royal Serbian Academy,
350   Belgrade, 1–633 pp.1941.

Sewall, J. O., van de Wal, R. S. W., van der Zwan, K., van Oosterhout, C., Dijkstra, H. A., and Scotese, C. R.: Climate model boundary conditions for four Cretaceous time slices, Clim. Past, 3, 647–657, 10.5194/cp-3-647-2007, 2007.

Shi, Z. G., Liu, X. D., Sun, Y. B., An, Z. S., Liu, Z., and Kutzbach, J.: Distinct responses of East Asian summer and winter monsoons to astronomical forcing, Clim. Past, 7, 1363–1370, 10.5194/cp-7-1363-2011, 2011.

355   Thomson, D. J.: Spectrum estimation and harmonic analysis, Proceedings of the IEEE, 70, 1055–1096, 10.1109/proc.1982.12433, 1982.

Tian, M., Zhang, M., Ren, Y., Qiao, X., Wan, C., and Liu, P.: On the Sporopollen-Alga Assemblages and Environments from the Third Member of Nenjiang Formation in the Xinzhan Area of Songliao Basin, Journal of Jilin University (Earth Science Edition), 34, 449–455, 10.13278/j.cnki.jjuese.2005.04.007, 2005.

360 Wan, X., Zhao, J., Scott, R. W., Wang, P., Feng, Z., Huang, Q., and Xi, D.: Late Cretaceous stratigraphy, Songliao Basin, NE China: SK1 cores, Palaeogeography, Palaeoclimatology, Palaeoecology, 385, 31–43, 10.1016/j.palaeo.2012.10.024, 2013.

Wang, C., Feng, Z., Zhang, L., Huang, Y., Cao, K., Wang, P., and Zhao, B.: Cretaceous paleogeography and paleoclimate and the setting of SKI borehole sites in Songliao Basin, northeast China, Palaeogeography, Palaeoclimatology,
365 Palaeoecology, 385, 17–30, 10.1016/j.palaeo.2012.01.030, 2013.

Wang, P., Gao, Y., Cheng, R., Wang, G., Wu, H., Wan, X., Yang, G., and Wang, Z.: Centimeter-scale sedimentary sequence description of Upper Cretaceous Nenjiang Formation(upper numbers 3-5): Lithostratigraphy,facies and cyclostratigraphy,based on the scientific drilling(SK1) borehole in the Songliao Basin, Earth Science Frontiers, 18, 218–262, 2011.

370 Wang, T., Ramezani, J., Wang, C., Wu, H., He, H., and Bowring, S. A.: High-precision U–Pb geochronologic constraints on the Late Cretaceous terrestrial cyclostratigraphy and geomagnetic polarity from the Songliao Basin, Northeast China, Earth and Planetary Science Letters, 446, 37–44, 10.1016/j.epsl.2016.04.007, 2016.

Wu, H., Li, S., Wang, C., Chu, R., Wang, P., and Gao, Y.: Integrated chronostratigraphic framework for Cretaceous strata in the Songliao Basin, Earth Science Frontiers, 31, 431–445, 10.13745/j.esf.sf.2024.1.22, 2024.

375 Wu, H., Zhang, S., Hinnov, L. A., Jiang, G., Yang, T., Li, H., Wan, X., and Wang, C.: Cyclostratigraphy and orbital tuning of the terrestrial upper Santonian–Lower Danian in Songliao Basin, northeastern China, Earth and Planetary Science Letters, 407, 82–95, 10.1016/j.epsl.2014.09.038, 2014.

Wu, H. C., Zhang, S. H., Sui, S. W., and Huang, Q. H.: Recognition of Milankovitch cycles in the natural gamma-ray logging of Upper Cretaceous terrestrial strata in the Songliao Basin, Acta Geol Sin-Engl, 81, 996–1001, 2007.

380 Wu, H. C., Zhang, S. H., Jiang, G. Q., Hinnov, L., Yang, T., Li, H. Y., Wan, X. Q., and Wang, C. S.: Astrochronology of the Early Turonian-Early Campanian terrestrial succession in the Songliao Basin, northeastern China and its implication for long-period behavior of the Solar System, Palaeogeogr Palaeocl, 385, 55–70, 10.1016/j.palaeo.2012.09.004, 2013.

Xu, Z., Tang, C., Wei, J., Zeng, H., Xiao, P., and Liu, H.: Late Cretaceous palynological record and its paleoclimate significance in the southern of Daqing placanticline, North China Geology, 44, 74–80, 10.19948/j.12-1471/P.2021.02.10,
385 2021.

Yan, J., Xi, D., Yu, T., and Wan, X.: Biostratigraphy and paleoenvironmental change of the lower Nenjiang Formation in the Qingshankou area, Songliao Basin, Journal of Stratigraphy, 03, 296–302, 2007.

Yang, H., Huang, Y., Ma, C., Zhang, Z., and Wang, C.: Recognition of Milankovitch cycles in XRF core-scanning records of the Late Cretaceous Nenjiang Formation from the Songliao Basin (northeastern China) and their paleoclimate
390 implications, Journal of Asian Earth Sciences, 194, 10.1016/j.jseaes.2019.104183, 2020.

Yu, Z., He, H., Deng, C., Xi, D., Qin, Z., Wan, X., Wang, C., and Zhu, R.: New geochronological constraints for the Upper Cretaceous Nenjiang Formation in the Songliao Basin, NE China, Cretaceous Research, 102, 160–169, 10.1016/j.cretres.2019.05.006, 2019.

Zhao, J., Wan, X., Xi, D., Jing, X., Li, W., Huang, Q., and Zhang, J.: Late Cretaceous palynology and paleoclimate change:

395 Evidence from the SK1 (South) core, Songliao Basin, NE China, Science China Earth Sciences, 57, 2985–2997, 10.1007/s11430-014-4975-4, 2014.

Zhou, Z., Xi, D., Sun, L., Zhao, J., Yang, W., Ye, Y., Meng, X., and Wan, X.: Late Cretaceous (Santonian to Campanian) Palynological Records and Paleoclimatic Significance from Borehole ZKY2-1, Songliao Basin, Minerals, 13, 10.3390/min13030338, 2023.

400